Article:

Gerding, M, Daly, S and Plane, J (2019) Lidar soundings of the mesospheric nickel layer using Ni(^{3}F) and NI(^{3}D) transitions. Geophysical Research Letters, 46 (1). pp. 408-415.
ISSN: 0094-8276

https://doi.org/10.1029/2018GL080701

Lidar soundings of the mesospheric nickel layer using $Ni(^3F)$ and $Ni(^3D)$ transitions

M. Gerding[1], S. Daly[2], J. M. C. Plane[2]

[1]Leibniz-Institute of Atmospheric Physics at University Rostock, Kühlungsborn, Germany.
[2]School of Chemistry, University of Leeds, Leeds LS2 9JT, U.K.

Key Points:

- First observation of the mesospheric Ni layer from meta-stable $Ni(^3D)$ state revealed peak densities of $\sim 280-450\,\mathrm{cm}^{-3}$
- Compared to Fe and their respective abundance in CI-Chondrites, Ni is depleted by a factor of about two
- Observations hint at faster-than-expected conversion of Ni into ions and neutral reservoir molecules

Corresponding author: M. Gerding, gerding@iap-kborn.de

Corresponding author: J. M C. Plane, j.m.c.plane@leeds.ac.uk

Abstract

During six nights between January and March 2018 we observed the mesospheric Ni layer by lidar from Kühlungsborn, Germany (54°N, 12°E). For most of the soundings we utilized for the first time a transition from the low-lying excited Ni(^{3}D) state at 341 nm. For additional soundings we used the ground-state Ni(^{3}F) transition at 337 nm, giving similar results but a worse signal-to-noise ratio. We observed nightly mean Ni peak densities between ~280 and 450 cm^{-3} and column abundances between $3.1 \cdot 10^8$ cm^{-2} and $4.9 \cdot 10^8$ cm^{-2}. Comparing with iron densities we get a Fe/Ni ratio of 38, which is a factor of 2 larger than the ratio in CI-Chondrites and factor of 32 larger than the Fe/Ni ratio observed by the only previous measurement of mesospheric Ni [*Collins et al.*, 2015]. The underabundance of Ni compared to CI-Chondrites suggests that Ni is more efficiently sequestered as Ni^+ or neutral reservoir species than Fe.

1 Introduction

The mesospheric metal layers produced by meteoric ablation between 80 and 110 km were first detected ~90 years ago by Na airglow observations [*Slipher*, 1929]. Subsequently, resonance lidars have been used for active, altitude resolved soundings [*Bowman et al.*, 1969], and most recently satellite-borne spectrometers, detecting scattered sunlight or nightglow, have provided a near global coverage [e.g. *Gumbel et al.*, 2007]. So far the alkali metals sodium, lithium and potassium [e.g. *Qian and Gardner*, 1995; *Jegou et al.*, 1980; *Eska et al.*, 1998], alkaline earth metals calcium [e.g. *Granier et al.*, 1985; *Gerding et al.*, 2000] and magnesium [e.g. *Correira et al.*, 2008; *Langowski et al.*, 2015] as well as the transition metal iron [e.g. *Bills and Gardner*, 1990; *Alpers et al.*, 1993; *Chu et al.*, 2011] have been investigated. The metal ions Ca^+ and Mg^+ have also been observed by ground-based lidar [e.g. *Gerding et al.*, 2000] and from space [*Langowski et al.*, 2015], respectively. Just as in the case of FeO chemiluminescence produced by the reaction Fe and O_3 [*Saran et al.*, 2011; *Unterguggenberger et al.*, 2017], chemiluminescence from NiO has also been detected [*Evans et al.*, 2011]. Very recently, a first detection of atomic Ni by lidar was published by *Collins et al.* [2015] (in the following abbreviated as CLM2015). The major source of these metals is the ablation of interplanetary dust particles originating from comets and asteroids [*Carrillo-Sánchez et al.*, 2016]. However, it has been clear even from early soundings that the relative abundances of the metals in the mesospheric layers can be quite different from their relative abundances in CI-Chondrites

[*Plane*, 1991; *Gerding et al.*, 1999; *Raizada et al.*, 2004; *Höffner and Friedman*, 2005; *Yi et al.*, 2009]. Clearly, factors including differential ablation, chemistry and dynamics play important roles in determining the relative metal concentrations and their temporal and spatial variations [e.g. *Plane et al.*, 2015].

For a metallic species in the mesosphere to be detectable by lidar from the ground, the product of resonance backscatter cross section and metal density must be large enough to produce a sufficient signal-to-noise ratio (SNR). Furthermore, the wavelength needs to be in the transmission range of the atmosphere (i.e. at wavelengths longer than the ~300 nm cut-off caused by the stratospheric O_3 layer). For nickel, the expected signal should be weak, because the relative Ni abundance should be low based on their chondritic abundances, around 1/18 that of Fe [*Asplund et al.*, 2009]. In fact, the first and so far only observations of the Ni layer are reported by CLM2015 from Chatanika, Alaska (65°N, 147°W). The peak Ni concentration was found to be ~16,000 cm^{-3}. This is surprisingly large, within a factor of 2 of the Fe concentration measured at the same location and time of year.

In early 2018 we performed Ni observations during six nights at Kühlungsborn, Germany (54°N, 12°E), using Ni resonance transitions at 337 nm for ground-state Ni(^{3}F), and at 341 nm to probe the low-lying Ni(^{3}D) state (CLM2015 used only the 337 nm transition). In Section 2 we describe the lidar setup and the selection of resonance lines. The observations are presented in Section 3, followed by a discussion of the results (Section 4).

2 Lidar setup and selection of resonance lines

In order to produce laser emission at the Ni resonance wavelengths at $\lambda_{air} = 336.9563$ nm and $\lambda_{air} = 341.4764$ nm (see Fig. S1 in the Supporting Information (SI)), we used an excimer-pumped (XeCl) dye laser with a repetition rate of 30 pps, as described in *Gerding et al.* [2000], but here we combined it with a different receiver. As in CLM2015, we used p-Terphenyl (PTP) dye dissolved in p-Dioxane for operation at 337 nm or 341 nm [*Brackmann*, 1994]. The oscillator of the dye laser was equipped with an intracavity etalon to limit the spectral bandwidth to 0.4 pm. Using two amplifier stages the dye laser pulse energy was up to 4 mJ at 337 nm, and 14 mJ at 341 nm. For some soundings a wavemeter (High Finesse WS6-200) was used for wavelength calibration and adjustment. The backscattered light was collected by a 78 cm telescope and guided to the detection bench by a quartz fiber. The detector was equipped with a 29 nm (full width at half maximum) interference filter (IF) with ∼85% transmission at the two wavelengths, and a Hamamatsu R7600U-200 photomultiplier tube with ∼40% quantum efficiency. The comparatively wideband IF therefore required lidar soundings during moonless nights, but the high transmission together with the PMT specification resulted in a large SNR.

The first successful observations of the Ni layer above Kühlungsborn were made with the Ni(^{3}D) transition at $\lambda_{air} = 341.4764$ nm. This wavelength is closer to the emission maximum of the dye than the Ni(^{3}F) transition at $\lambda_{air} = 336.9563$ nm, yielding a better wavelength stability, less broadband emission, and larger laser power. Later on, we tuned the laser to the Ni(^{3}F) resonance line at 337 nm. Comparisons of the soundings at both transitions are presented in Section 3.3. The (effective) differential backscatter cross sections are calculated as described by *Fricke and von Zahn* [1985] and *Chu and Papen* [2005] using oscillator strengths of 0.12 for Ni(^{3}D) and 0.024 for Ni(^{3}F) [*Kramida et al.*, 2018]. This yields $\sigma_{res} = 1.08{\cdot}10^{-17}$ m^2/sr ($\sigma_{res} = 2.12{\cdot}10^{-18}$ m^2/sr) and $\sigma_{Ray} = 3.57{\cdot}10^{-31}$ m^2/sr ($\sigma_{Ray} = 3.75{\cdot}10^{-31}$ m^2/sr) for resonance and Rayleigh backscatter at 341 nm (337 nm), respectively. Numbers are given for 0.4 pm laser full width at half maximum (FWHM, assuming Lorentz shape) and 200 K atmospheric temperature at ∼90 km altitude in winter. Later on we used a corrected effective cross section for 337 nm, see Section 4. Note that the Ni(^{3}D) resonance cross section is about five times larger than that for Ni(^{3}F). The Ni densities at altitude z are calculated as usual by the equation

$$\rho_{Ni}(\mathrm{z}) = \rho_{air}(z_R) \cdot \sigma_{Ray}/\sigma_{res} \cdot N^{corr}_{res}(z)/N^{corr}_{Ray}(z_R)$$

with N^{corr}_{res} the range-corrected resonance count rate, $N^{corr}_{Ray}(z_R)$ the range-corrected Rayleigh count rate at the reference altitude, $\rho_{air}(z_R)$ air density at the reference altitude taken from NRLMSISE-00 [*Picone et al.*, 2002], and z_R reference altitude chosen as 50 km, i.e. avoiding corrections for stratospheric aerosol backscatter and ozone absorption. An additional factor is then applied which takes account of the thermal populations of the $^3D_3$ and $^3F_4$ states used here. At typical upper mesospheric temperature of 200 K these are 15.1 and 84.9%, respectively. The calculation of these fractions is explained in the SI. The fraction of $^3D_3$ is temperature dependent, and given by the expression $0.570 \cdot exp(-265.8/T)$. Simultaneous temperature soundings with the IAP RMR lidar [*Gerding et al.*, 2016] revealed temperatures varying with time between 180 and 220 K in the peak region of the Ni layer at 85 km (not shown). Climatological data for higher altitudes has been published by *Gerding et al.* [2008], showing that similar temperatures can be expected for the whole range of the Ni layer and the whole Jan-March period. For these temperatures the fraction of Ni($^3D_3$) varies from 13.1 to 17.0%. Not having direct temperature measurements available for the whole altitude range, we assume a constant fraction of 15.1%. Additionally, for density calculations the relaxation of the ^3F transition via a 380.7 nm emission is acknowledged with 7% probability (see Figure S1 in the SI). All other relevant relaxations are within the transmission range of the IF, in particular at 339.3 nm and 347.3 nm for the excitation of Ni(^3F), and at 339.1 nm for the excitation of Ni(^3D) [cf. *Kramida et al.*, 2018].

Overall we expect a similar resonance signal for the Ni(^3D) transition compared to the Ni(^3F) transition used by CLM2015 if the laser power is the same at both wavelengths. Photon counts were collected in 200 m bins and further integrated to 1 km in order to improve the SNR. Statistical uncertainties of the Ni density profiles are calculated based on Poisson statistics for these 1 km bins.

Similar to CLM2015 we did not have an absolute wavelength reading available for most of the soundings. Only for the soundings in March 2018 were we able to measure the wavelength of the pulsed light in the lab (see below). Wavelength adjustment using only the laser keypad interface has an unknown bias of 30 − 50 pm. Therefore, for the first successful soundings in January 2018, we rapidly scanned the dye laser over a wide range of ∼100 pm and continuously checked the backscatter signal as well as recording the data for later analysis. After a coarse adjustment the final wavelength was found in a detailed scan across ∼1 pm based on the normalized resonance backscatter after integration of 4000 laser pulses (∼2.5 min) and 0.2 pm wavelength steps per profile. For the next sounding nights typically only the fine tuning needed to be repeated, because we kept the laser electronics running continuously and the laser temperature stabilized. During the soundings, the wavelength was checked about once per hour to avoid wavelength drifts due to thermal adjustment of the laser resonator. Similarly, the bandwidth of the pulsed laser was checked about once per hour by inspection of the transmission of an external monitoring etalon.

In March 2018 we measured the true laser wavelength with the WS6-200 wavelength meter. This wavemeter has an absolute accuracy of 0.2 pm in our wavelength range, which is in the range of the bandwidth of the pulsed laser. The optimal wavelength was cross-checked by the atmospheric return. We used the WS6-200 both for the observation of the Ni(^{3}D) transition at 341 nm as well as for the Ni(^{3}F) transition at 337 nm.

3 Observations at 341 nm and 337 nm

Nickel soundings at Kühlungsborn were made successfully during six nights in January to March 2018. Further off-resonance soundings were made beforehand for initial tests. In this section we present examples of the raw data obtained at 341 nm and 337 nm as well as the calculated density profiles for all data.

3.1 Raw data with and without background 8/9 January 2018

First observations of the mesospheric Ni layer above Kühlungsborn were made during the night 7/8 January 2018. The laser was operated at the resonance wavelength $\lambda_{air} = 341.4764$ nm for 40 min (72,000 laser pulses). In the following night, we observed the Ni layer for ∼2.5 h at the same transition. Figure 1 shows the integrated raw data **Fig.1** profile with and without the background count rate. Above 50 km the molecular backscatter (Rayleigh signal) is visible, decreasing with altitude due to decreasing air density. Above ∼78 km the signal clearly increases due to the additional resonance backsscatter. The nickel layer can be observed up to ∼100 km. At higher altitudes the constant background count rate is due to detector noise and sky background (∼1400 counts/km). After background subtraction the Ni layer is even more clearly identified. Above 78 km the profile shows initially a superposition of the comparatively intense Rayleigh signal and the resonance signal. At the altitude of the maximum of the Ni layer, ∼200 photons/km are counted from the Rayleigh signal and 2400 photons/km are due to resonance backscatter. We extrapolate the range-corrected Rayleigh signal above 76 km with a normalized nightly NRLMSISE-00 density profile [*Picone et al.*, 2002], and subtract this data to get a pure resonance count rate (not shown).

3.2 Ni density profiles observed at 341 nm wavelength

The integrated, range-corrected and Rayleigh-subtracted backscatter profiles are used to calculate a mean Ni density profile. The statistical uncertainty is taken as the square root of the original count rate (with 1 km resolution) assuming Poisson statistics. In Figure 2 the Ni density profile on the evening 8 Jan 2018 is presented by the blue line, **Fig.2**

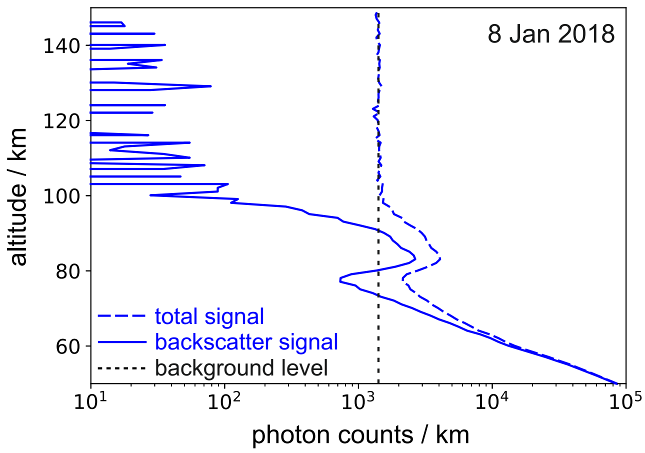

Figure 1. Integrated raw data profile for the evening 8 January 2018 before and after background subtraction. The altitude resolution is set to 1 km.

with the dotted line showing the statistical uncertainty. The Ni layer extends from 78 km to more than 100 km altitude. The maximum is observed at 84 km with a peak density of ∼280 cm^{-3}, and a vertical column abundance of $3.3 \cdot 10^8$ cm^{-2}. Fig. 2 also shows the other four Ni density profiles measured using the $Ni(^3D)$ resonance at 341 nm. These profiles were obtained from observational periods ranging from 0.65 to 3.5 h. The peak densities vary between ∼280 cm^{-3} (8 Jan and 20 Mar 2018) and ∼450 cm^{-3} (7 Jan 2018). The lower edges of the Ni layer vary by as much as 5 km between the nights. The layer shape often differs from an ideal Gaussian and the peak height varies by ∼3 km.

The long sounding and high signal level on 8/9 January 2018 reveals the temporal evolution of the Ni layer for the first time. Figure 3 shows that during the 3.5 h of **Fig.3**
lidar observation the layer was highly variable. The peak density varies by up to 50% and the peak altitude partly changes by 2 km within only ∼15 min. The lower edge of the layer ascends slowly by 2 km from 78 to 80 km. On the topside of the layer the variability is larger and occurs on shorter scales. Overall, even though this is only a single observation, the variability of the Ni layer seems to be larger compared to the Fe layer, which is surprising given that both are transition metals and thus might to a first approximation be expected to behave similarly.

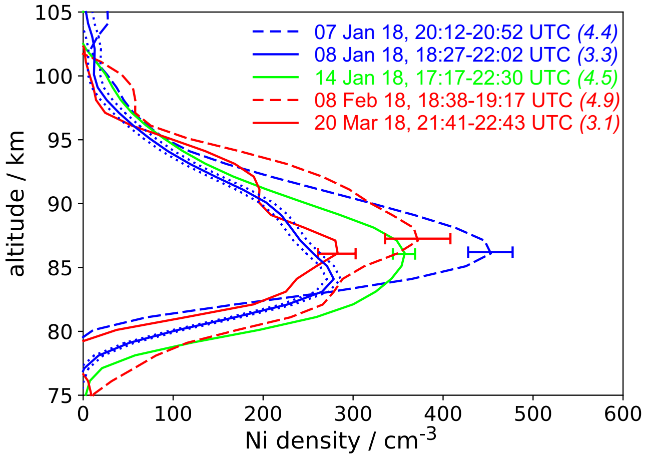

Figure 2. Nickel density profiles for all measurements using the Ni(^{3}D) transition at 341 nm. Uncertainties (dotted lines or error bars at the layer maximum) calculated for the original resolution of 1 km. Profiles are smoothed by 7-point Hann windows for visualization only. Numbers in brackets denote vertical column abundances in units of 10^8 cm^{-2}.

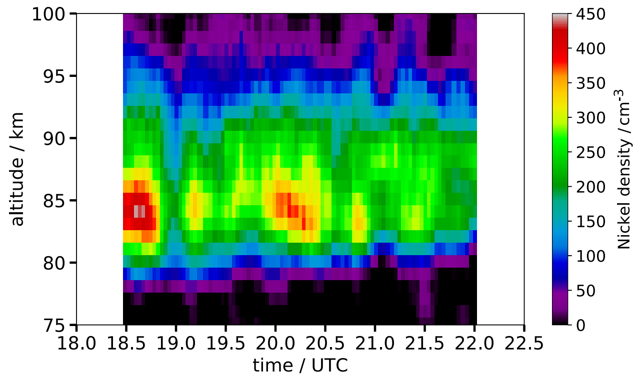

Figure 3. Temporal evolution of the nickel layer during the 3.5 h long sounding on 8 Jan 2018. Data are plotted with a 5-profile sliding average (20,000 pulses) and vertical smoothing using a 7-bin Hann window.

3.3 Observations at 337 and 341 nm

After successful nickel soundings using the Ni(^{3}D) transition at 341 nm we tuned the laser to the Ni(^{3}F) transition at 337 nm in order to make soundings at the same wavelength as CLM2015. Because of the lower laser pulse energy the Rayleigh signal is weaker here. As mentioned above, the backscatter cross section of the Ni(^{3}F) transition is smaller, but the fraction of atoms in the ground state is larger. Overall, a similar signal to that at 341 nm would be expected. Making use of the WS6-200 wavemeter we were able to adjust the laser to the Ni(^{3}F) transition and receive a resonance signal from the mesopause region. The first soundings were performed for 2.5 h in the night 18/19 March 2018. Nickel densities were found to be lower than for Jan/Feb observations (not shown).

Two nights later on 20/21 March 2018 we made comparative soundings at both wavelengths sequentially. First, we set the laser to the Ni(^{3}F) resonance at 337 nm and collected data between 19:04 and 21:22 UTC (236,000 pulses). After that we tuned the laser back to 341 nm and recorded data for another hour (21:41–22:43 UTC). Figure 4 (top) **Fig.4** shows the integrated raw data profiles for both periods after background subtraction and range correction. For 337 nm the uncorrected profile with background is also displayed. Similar to the raw data shown by CLM2015, the 337 nm resonance backscatter is quite weak and hardly visible on top of the background. (Note the stronger smoothing of the CML2015 data.) In contrast to this, the 341 nm resonance signal was similar to the sounding on 8 Jan 2018, taking the shorter integration time into account (see Fig. 1). The Rayleigh signals at 337 and 341 nm reflect the differences in laser power (1:3) and integration time (2:1), but still the resonance signal at 337 nm is smaller then expected from 341 nm.

However, before calculating the Ni density for the sounding at 337 nm, some technical limitations need to be acknowledged. In contrast to the sounding at 341 nm we assume here a 33% fraction of Amplified Spontaneous Emission (ASE) and a de-tuning of the laser wavelength of 0.1 pm (cf. Section 4). The resulting density profiles are shown in Figure 4 (bottom). For most of the altitudes they agree within their uncertainties. The general structure of the profiles is similar with a maximum around 85 km and a "shoulder" between 90 and 95 km. Nevertheless, the first profile shows about 30% lower densities than the second profile. These differences are within the temporal variability of the Ni layer displayed in Fig. 3.

4 Discussion and Conclusion

We have detected atomic Ni as a layer in the middle atmosphere with peak densities between ∼280 and 450 cm^{-3} and column abundances between $3.1{\cdot}10^8$ cm^{-2} and $4.9{\cdot}10^8$ cm^{-2}. There are numerous publications on observations of the mesospheric Na, K, Mg, Ca and Fe layers, differences of the relative metal abundance to their Chrondritic ratios, and the related chemistry (see, e.g., the review by *Plane et al.* [2015]). In

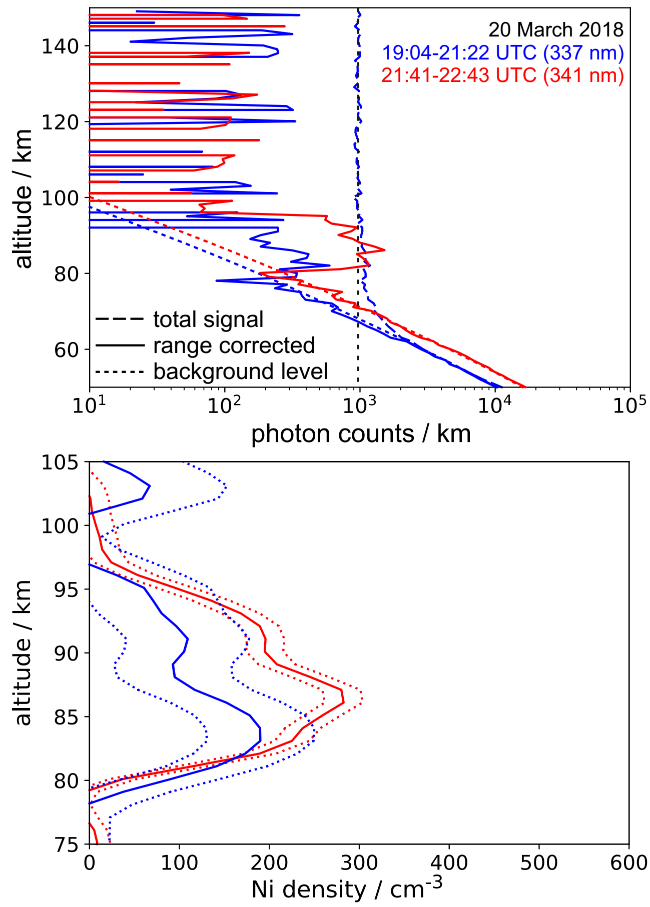

Figure 4. top: Raw data profile of Ni soundings on 20 Mar 2018 with background (dashed) and after background subtraction and additional range correction (solid). Dotted red/blue line: Normalized NRLMSISE-00 density profile used for Rayleigh subtraction. Blue: 337 nm, red: 341 nm, black: background level of 337 nm data. bottom: Ni density profiles calculated from the raw data. Uncertainties and smoothing as in Fig. 2.

contrast, before the present study there is only one previous observation of the nickel layer published by CLM2015, showing peak densities of $\sim$16,000 cm^{-3} and column densities of $2.7 \cdot 10^{10}$ cm^{-2}. These numbers are a factor of 50–70 larger than the densities derived here. In the following we discuss our observations and potential reasons for the disagreement with CLM2015.

For the first attempts to detect the Ni layer using the Ni(^{3}F) transition at 337 nm, the dye laser was operated without the intracavity etalon that we used later to limit the laser linewidth. This configuration was in fact similar to the setup used by CLM2015. Unfortunately we failed to detect a resonance signal while scanning the laser wavelength.

We noted a large variability of the Rayleigh signal level during the first trials, presumably due to changing atmospheric humidity that affects the aerosol properties, i.e. visibility in the UV. The signal level decreased in some nights by a factor of 100, while the simultaneous soundings of the RMR lidar at 532 nm [*Gerding et al.*, 2016] essentially showed no change. During the nights of normal signal level we detected the Rayleigh signal well into the altitude of the metal layer (cf. Fig. 4), i.e. much higher than observed by CLM2015. Therefore, the lidar soundings in the present study should have a much higher SNR.

It turned out that the laser performed much better at 341 nm, i.e. at the resonance transition of the low-lying Ni(^{3}D) metastable state. We were able to assemble the intracavity etalon, narrowing the laser linewidth. Based on the laser adjustment made, it was possible later to tune the laser to 337 nm even with the intracavity etalon. Finally, the wavemeter assured a much better wavelength tuning of laser, and also weak resonance backscatter was sufficient for Ni density measurements.

We now consider several reasons why our soundings might have yielded Ni densities that are so much smaller than CLM2015. First, the laser might not have been tuned to the center of the resonance line. However, we carefully checked the wavelength by manual changes in steps of 0.2 pm. We clearly identified the largest backscatter counts from the metal layer and then set the wavelength appropriately. These checks were repeated regularly, so we estimate the potential systematic error to be only 0.2 pm, resulting in a potential underestimation of the true density by at most 25%. Second, the laser output may have had a large fraction of broadband emission that contributed to the Rayleigh signal but not to the resonance signal. However, we regularly checked the bandwidth of the laser and the fraction of broadband emission throughout the sounding by means of an external etalon. In later soundings, the wavemeter provided some additional evidence that most of the laser emission was narrowband. Third, the overlap between laser beam and telescope field of view might have decreased with altitude. However, the overlap was regularly checked at 30 km altitude where the SNR is large. For higher altitudes we checked the overlap based on the nightly integrated data by comparison with the RMR lidar signal obtained simultaneously. No significant difference was found. We do not have any indications for further systematic errors due to laser performance and therefore assess an additional underestimation of the Ni density being smaller than the potential error due to incorrect tuning of the laser wavelength. Finally, we consider that the Ni densities published here are reliable within the stated uncertainties.

As mentioned above, the laser performance at 337 is worse compared to 341 nm which is closer to the fluorescence maximum of the PTP dye at 343 nm [*Brackmann*, 1994]. Therefore, operation of the laser at 337 nm is more sensitive to misalignment etc. Indeed, during the soundings at 337 nm we noticed a poorer contrast of the ring system produced by the external monitoring etalon. Also the wavemeter indicated a larger fraction of broadband emission, although this is difficult to quantify because of the design of the instrument. Regarding a potential offset of the laser wavelength with respect to the resonance line it should be noted that the spectral resolution of the wavemeter WS6-200 is 0.2 pm (at 337 nm), and a potential offset of the laser of 0.1 pm is still smaller than the expected accuracy of manual scanning of the laser based on atmospheric return. Taking both effects into account (33% broadband emission and 0.1 pm offset), we estimate an effective differential backscatter cross section at 337 nm of $1.42 \cdot 10^{-18}\,\mathrm{m^2/sr}$. This is already taken into account in the density calculations (see Fig. 4, bottom).

One unexpected result of the present study is that a much better lidar resonance signal is achieved by monitoring the metastable ^{3}D state at 341 nm. This is the first example of a metal resonance lidar where this is the case. It is therefore worth considering whether the ^{3}D and ^{3}F states are likely to be in thermal equilibrium, which we have assumed when calculating their relative populations (see the SI). Like the other meteoric metals [*Plane et al.*, 2015], Ni should exist in a fast chemical steady state with NiO, controlled by the reactions of Ni with O_3 and NiO with O. The latter reaction could produce Ni in a non-Boltzmann population initially. However, taking a recently measured rate coefficient $k(\mathrm{Ni} + \mathrm{O_3} \rightarrow \mathrm{NiO} + \mathrm{O_2}) = (6.5 \pm 0.7) \cdot 10^{-10}\,\mathrm{cm^3\ molecule^{-1}\ s^{-1}}$ [T. P. Mangan, University of Leeds, pers. comm.] and a typical O_3 concentration at 85 km of $5 \cdot 10^8\,\mathrm{cm^{-3}}$, the e-folding time for Ni conversion to NiO will be $\sim$3.1 s. During this time the Ni atom will experience on the order of 10^5 collisions with air molecules and, given that the separation of the ^{3}D and ^{3}F states is only $204.8\,\mathrm{cm^{-1}}$, it is very likely that these states will be fully equilibrated.

Finally, we consider the Ni vertical column abundance of $4.0 \cdot 10^8\,\mathrm{cm^{-2}}$ in the context of the well-studied mesospheric Fe layer. A typical Fe column abundance in January-March at mid-latitudes is $1.5 \cdot 10^{10}\,\mathrm{cm^{-2}}$ [*Kane and Gardner*, 1993], which implies a Fe/Ni ratio around 38. This ratio is about a factor of 2 larger than the Fe/Ni ratio of 18 in CI-Chondrites [*Asplund et al.*, 2009]. Since Ni mainly resides in meteorites as Ni-Fe-S grains which melt at a lower temperature than the Fe-containing silicate phase [*Levasseur-Regourd et al.*, 2018], it is unlikely that Ni will ablate less efficiently than Fe. Therefore the 2-fold depletion of Ni indicates that Ni is more efficiently sequestered as Ni^+ or neutral reservoir species, compared with Fe. Studies of the relevant Ni kinetics are currently underway at Leeds, in an attempt to understand this.

The Fe/Ni ratio of 1.2 published by CLM2015, i.e. a factor of 22 smaller than the CI ratio, is even more difficult to account for as those authors recognized. There is no obvious explanation for the factor of $50-70$ discrepancy (in absolute density, or factor of $\sim$40 in Fe/Ni) between our observations and those of CLM2015. We cannot exclude latitudinal differences, but these would have to be surprisingly large: typically, metal abundances increase by no more than a factor of 2 between mid- and high-latitudes [*Feng et al.*, 2013; *Langowski et al.*, 2015]. Future soundings, using the comparatively easy-to-reach transition at 341 nm suggested here, may help to resolve this discrepancy. Preferably, these should be conducted simultaneously with co-located Fe soundings.

Acknowledgments

We thank our colleagues Torsten Köpnick and Reik Ostermann for their help with the lidar electronics, Josef Höffner for provision of the data aquisition software, and Michael Priester for his help for maintaining the laser. We acknowledge funding from the UK Natural Environment Research Council (grant number NE/P001815/1). SMD has a research studentship funded by the NERCs SPHERES doctoral training programme. Lidar data are available at ftp://ftp.iap-kborn.de/data-in-publications/ GerdingGRL2018/.

References

Alpers, M., T. Blix, S. Kirkwood, D. Krankowsky, F.-J. Lübken, S. Lutz, and U. von Zahn (1993), First simultaneous measurements of neutral and ionized iron densities in the upper mesosphere, *J. Geophys. Res.*, *98*, 275–283.

Asplund, M., N. Grevesse, A. J. Sauval, and P. Scott (2009), The chemical composition of the Sun, *Annual Review of Astronomy and Astrophysics*, *47*(1), 481–522, doi:10.1146/annurev.astro.46.060407.145222.

Bills, R. E., and C. S. Gardner (1990), Lidar observations of mesospheric Fe and sporadic Fe layers at Urbana, Illinois, *Geophys. Res. Lett.*, *17*, 143–146, doi: 10.1029/GL017i002p00143.

Bowman, M. R., A. J. Gibson, and M. C. W. Sandford (1969), Atmospheric sodium measured by a tuned laser radar, *Nature*, *221*, 456–457, doi:10.1038/221456a0.

Brackmann, U. (1994), *Lambdachrome laser dyes*, Lambda Physik GmbH, Goettingen, Germany.

Carrillo-Sánchez, J. D., D. Nesvorný, P. Pokorný, D. Janches, and J. M. C. Plane (2016), Sources of cosmic dust in the Earth's atmosphere, *Geophys. Res. Lett.*, *43*(23), 11,979–11,986, doi:10.1002/2016GL071697.

Chu, X., and G. C. Papen (2005), *Resonance fluorescence lidar for measurements of the middle and upper atmosphere*, CRC Press, Boca Raton, USA.

Chu, X., Z. Yu, C. S. Gardner, C. Chen, and W. Fong (2011), Lidar observations of neutral Fe layers and fast gravity waves in the thermosphere (110-155 km) at McMurdo (77.8°S, 166.7°E), Antarctica, *Geophys. Res. Lett.*, *38*, L23807, doi: 10.1029/2011GL050016.

Collins, R. L., J. Li, and C. M. Martus (2015), First lidar observation of the mesospheric nickel layer, *Geophys. Res. Lett.*, *42*, 665–671, doi:10.1002/2014GL062716.

Correira, J., A. C. Aikin, J. M. Grebowsky, W. D. Pesnell, and J. Burrows (2008), Seasonal variations of magnesium atoms in the mesosphere-thermosphere, *Geophys. Res. Lett.*, *35*, L06103, doi:10.1029/2007GL033047.

Eska, V., J. Höffner, and U. von Zahn (1998), Upper atmosphere potassium layer and its seasonal variations at 54° N, *J. Geophys. Res.*, *103*(A12), 29,207–29,214, doi:10.1029/98JA02481.

Evans, W. F. J., R. L. Gattinger, A. L. Broadfoot, and E. J. Llewellyn (2011), The observation of chemiluminescent NiO* emissions in the laboratory and in the night airglow, *Atmos. Chem. Phys.*, *11*(18), 9595–9603, doi:10.5194/acp-11-9595-2011.

Feng, W., D. R. Marsh, M. P. Chipperfield, D. Janches, J. Höffner, F. Yi, and J. M. C. Plane (2013), A global atmospheric model of meteoric iron, *J. Geophys. Res.*, *118*(16), 9456–9474, doi:10.1002/jgrd.50708.

Fricke, K., and U. von Zahn (1985), Mesopause temperatures derived from probing the hyperfine structure of the D2 resonance line of sodium by lidar, *J. Atmos.*

Solar-Terr. Phys., *47*(5), 499 – 512, doi:10.1016/0021-9169(85)90116-3.

Gerding, M., M. Alpers, J. Höffner, and U. von Zahn (1999), Simultaneous K and Ca lidar observations during a meteor shower on March 6-7, 1997, at Kühlungsborn, Germany, *J. Geophys. Res.*, *104*, 24,689–24,698.

Gerding, M., M. Alpers, U. von Zahn, R. J. Rollason, and J. M. C. Plane (2000), Atmospheric Ca and Ca^+ layers: Midlatitude observations and modeling, *J. Geophys. Res.*, *105*(A12), 27,131–27,146, doi:10.1029/2000JA900088.

Gerding, M., J. Höffner, J. Lautenbach, M. Rauthe, and F.-J. Lübken (2008), Seasonal variation of nocturnal temperatures between 1 and 105 km altitude at 54°N observed by lidar, *Atmos. Chem. Phys.*, *8*, 7465–7482.

Gerding, M., M. Kopp, J. Höffner, K. Baumgarten, and F.-J. Lübken (2016), Mesospheric temperature soundings with the new, daylight-capable IAP RMR lidar, *Atmos. Meas. Tech.*, *9*(8), 3707–3715, doi:10.5194/amt-9-3707-2016.

Granier, C., J. P. Jegou, and G. Megie (1985), Resonant lidar detection of Ca and Ca^+ in the upper atmosphere, *Geophys. Res. Lett.*, *12*, 655–658, doi: 10.1029/GL012i010p00655.

Gumbel, J., Z. Y. Fan, T. Waldemarsson, J. Stegman, G. Witt, E. J. Llewellyn, C.-Y. She, and J. M. C. Plane (2007), Retrieval of global mesospheric sodium densities from the Odin satellite, *Geophys. Res. Lett.*, *34*(4), L04813, doi: 10.1029/2006GL028687.

Höffner, J., and J. S. Friedman (2005), The mesospheric metal layer topside: Examples of simultaneous metal observations, *J. Atmos. Solar-Terr. Phys.*, *67*(13), 1226 – 1237, doi:10.1016/j.jastp.2005.06.010.

Jegou, J.-P., M.-L. Chanin, G. Mégie, and J. E. Blamont (1980), Lidar measurements of atmospheric lithium, *Geophys. Res. Lett.*, *7*(11), 995–998, doi: 10.1029/GL007i011p00995.

Kane, T. J., and C. S. Gardner (1993), Structure and seasonal variability of the nighttime mesospheric Fe layer at midlatitudes, *J. Geophys. Res.*, *98*, 16, doi: 10.1029/93JD01225.

Kramida, A., Yu. Ralchenko, J. Reader, and and NIST ASD Team (2018), NIST Atomic Spectra Database (ver. 5.5.6), [Online]. Available: `https://physics.nist.gov/asd` [2018, September 20]. National Institute of Standards and Technology, Gaithersburg, MD.

Langowski, M. P., C. von Savigny, J. P. Burrows, W. Feng, J. M. C. Plane, D. R. Marsh, D. Janches, M. Sinnhuber, A. C. Aikin, and P. Liebing (2015), Global investigation of the Mg atom and ion layers using SCIAMACHY/Envisat observations between 70 and 150 km altitude and WACCM-Mg model results, *Atmos. Chem. Phys.*, *15*(1), 273–295, doi:10.5194/acp-15-273-2015.

Levasseur-Regourd, A.-C., J. Agarwal, H. Cottin, C. Engrand, G. Flynn, M. Fulle, T. Gombosi, Y. Langevin, J. Lasue, T. Mannel, S. Merouane, O. Poch, N. Thomas, and A. Westphal (2018), Cometary dust, *Space Science Reviews*, *214*(3), 64, doi:10.1007/s11214-018-0496-3.

Picone, J. M., A. E. Hedin, D. P. Drob, and A. C. Aikin (2002), NRLMSISE-00 empirical model of the atmosphere: Statistical comparison and scientific issues, *J. Geophys. Res.*, *107*(A12), 1468, doi:10.1029/2002JA009430.

Plane, J. M. C. (1991), The chemistry of meteoric metals in the Earth's upper atmosphere, *International Reviews in Physical Chemistry*, *10*(1), 55–106, doi: 10.1080/01442359109353254.

Plane, J. M. C., W. Feng, and E. C. M. Dawkins (2015), The mesosphere and metals: Chemistry and changes, *Chemical Reviews*, *115*(10), 4497–4541, doi: 10.1021/cr500501m.

Qian, J., and C. S. Gardner (1995), Simultaneous lidar measurements of mesospheric Ca, Na, and temperature profiles at Urbana, Illinois, *J. Geophys. Res.*, *100*, 7453–7461, doi:10.1029/94JD02748.

Raizada, S., C. A. Tepley, D. Janches, J. S. Friedman, Q. Zhou, and J. D. Mathews (2004), Lidar observations of Ca and K metallic layers from Arecibo and comparison with micrometeor sporadic activity, *J. Atmos. Solar-Terr. Phys.*, *66*, 595–606, doi:10.1016/j.jastp.2004.01.030.

Saran, D. V., T. G. Slanger, W. Feng, and J. M. C. Plane (2011), FeO emission in the mesosphere: Detectability, diurnal behavior, and modeling, *J. Geophys. Res.*, *116*, D12303, doi:10.1029/2011JD015662.

Slipher, V. M. (1929), Emissions in the spectrum of the light of the night sky, *Publ. Astron. Soc. Pac.*, *41*, 262265.

Unterguggenberger, S., S. Noll, W. Feng, J. M. C. Plane, W. Kausch, S. Kimeswenger, A. Jones, and S. Moehler (2017), Measuring FeO variation using astronomical spectroscopic observations, *Atmos. Chem. Phys.*, *17*(6), 4177–4187, doi:

10.5194/acp-17-4177-2017.

Yi, F., C. Yu, S. Zhang, X. Yue, Y. He, C. Huang, Y. Zhang, and K. Huang (2009), Seasonal variations of the nocturnal mesospheric Na and Fe layers at 30°N, *J. Geophys. Res.*, *114* (D1), D01301, doi:10.1029/2008JD010344.